Exploring the hydrogen evolution reaction performance on a borophene monolayer

Jing Liu^{1,*} and Axel Groß^{1,†}

¹Institute of Theoretical Chemistry, Ulm University,
Mez-Starck-Haus, Oberberghof 7, 89081 Ulm, Germany
(Dated: October 7, 2025)

Borophene, a unique two-dimensional boron-based material with a graphene-like structure, has attracted growing interest due to its special configurations and remarkable physical and chemical properties. This study focuses on four different borophene phases: α , $\beta12$, $\gamma3$, and trigonal, and systematically investigates their hydrogen evolution reaction (HER) performance. By using density functional theory (DFT), we evaluate the intrinsic catalytic activity of pristine borophene monolayers as well as the influence of an Ag(111) substrate on their HER behavior. The results indicate that the pristine α , $\beta12$, and $\gamma3$ phases exhibit excellent HER activity, characterized by optimal Gibbs free energies for hydrogen adsorption. Especially, the on-top site with the lowest coordination number is identified as the most active site. However, interaction with the Ag(111) support significantly modifies the hydrogen binding, leading to suppressed HER performance in these phases. In contrast, the trigonal phase displays relatively poor HER performance, attributed to its fully saturated bonding environment, while the silver substrate significantly modifies its geometric configuration and slightly enhances the HER performance. This work highlights both the promising intrinsic HER potential of borophene monolayers and the critical impact of substrate interactions, guiding the design of efficient borophene-based electrocatalysts.

INTRODUCTION

Low-dimensional materials have attracted extensive research interest due to their unique physical and chemical properties, which often differ significantly from their bulk counterparts [1–6]. As is well known, carbon already plays an important role in the formation of low-dimensional materials, giving rise to a variety of well-known allotropes across different dimensions, namely 0-dimensional fullerenes [7– 10], 1-dimensional carbon nanotubes [11–13], and 2-dimensional graphene [14–18], each exhibiting distinct electronic and mechanical properties. Graphene has emerged as a prototype 2D material due to its exceptional properties, such as ultrahigh carrier mobility, superior mechanical strength, and excellent thermal conductivity [19–21]. These remarkable properties lead to its widespread applications in nanoelectronics, energy storage, and catalysis [20, 22–26]. Given the success of carbon-based materials, it naturally raises the question: Are there other elements, particularly those near carbon in the periodic table, that could form similar low-dimensional structures? this regard, stands out as one of the most promising elements. Its unique bonding flexibility allows it to form diverse low-dimensional configurations, such as boron buckyballs [27–30], boron nanotubes [31–33], and boron sheets [34–36].

In particular, the atomically thin 2-D boron sheet, so-called borophene, has first been synthesized on Ag(111) surface, inspiring a wide interest in investigations on the 2-D boron structures[35, 37, 38]. For instance, Kiraly et al. successfully synthesized and characterized nanoscale borophene on Au(111) in

UHV [39]. Li et al. reported a graphene-like honeycomb borophene structure grown on an Al(111) surface via molecular beam epitaxy under ultrahigh vacuum conditions [40]. Wu et. al. successfully grew borophene on Cu(111) surfaces, obtaining large single-crystal domains with sizes up to $100\,\mu\mathrm{m}^2$ [41]. Recent theoretical studies have also revealed the exfoliation mechanism of borophene, showing that high-density stacking faults in β -rhombohedral boron can significantly lower the exfoliation energy barrier, thus facilitating the formation of boron sheets [42]. This mechanism enhances the understanding of borophene synthesis and, in the meantime, makes borophene more promising for future applications.

Unlike the carbon atom, the unique electronic configuration of boron favors the formation of 2-dimensional lattices composed of triangular and hexagonal motifs, leading to a richer variety of structures compared to graphene, including the α , β 12, γ 3 phases, and others [34, 43–49]. Previous theoretical studies have shown that most borophene structures exhibit metallic behavior and, in certain structures, display a Dirac feature analogous to that in graphene [35, 50, 51]. These electronic characteristics, combined with the good carrier mobility, indicate that borophene can serve as an efficient electrode material [52, 53]. In addition, several studies have demonstrated the notable electrocatalytic properties of various boron sheets [54–59]. Considering the relatively low cost of boron, these materials exhibit great potential as alternatives to traditional noble-metal catalysts, such as platinum [60]. In this work, we investigate the hydrogen evolution reaction (HER) on borophene using first-principles calculations. Four different borophene phases (α , β 12, γ 3, and trigonal) are analyzed to determine their catalytic activity, with a

focus on optimized structures, potential energy surface, and adsorption energy. Furthermore, the impact of metal substrates on HER performance is also explored, shosing that the adsorption behavior on free-standing two-dimensional sheets can be significantly altered when these sheets are supported by a metallic substrate. Our findings provide insights into the potential of borophene-based materials for electrocatalysis.

COMPUTIONAL DETAILS

We conducted first-principles calculations using density functional theory (DFT) as implemented Vienna Ab initio Simulation Package (VASP) [61, 62]. The projector augmented wave (PAW) method was adopted to treat the interaction between valence electrons and ionic cores Exchange-correlation interactions are described with the revised Perdew-Burke-Ernzerhof (RPBE) functional within the generalized gradient approximation (GGA), which provides an accurate estimate of the adsorption energetics, together with the D3 dispersion correction with Becke-Johnson damping (D3BJ) to account for long-range van der Waals interactions [64–67]. To ensure computational accuracy and convergence, we employed a plane-wave energy cutoff of 550 eV. A vacuum layer of 20 Å was introduced along the out-of-plane direction (z-axis) to eliminate artificial interactions between periodic images in the slab model. Full structural relaxations are performed until the total energy and atomic forces converge to thresholds of 10^{-4} eV/atom and 0.01 eV/Å, respectively. For Brillouin zone integration, a $5 \times 5 \times 1$ Monkhorst-Pack k-point mesh was used for the unit cell calculations. Based on the optimized structures, we further performed single-point total energy calculations with a higher level of precision. A denser $13 \times 13 \times 1$ k-point mesh was adopted to ensure accurate energy evaluation. For the electronic occupation, the zero-width Gaussian smearing was employed. Zero-point energy (ZPE) and thermal corrections were obtained using the post-processing package VASPKIT [68], based on finite-difference phonon calculations in VASP. The same $5 \times 5 \times 1$ Monkhorst-Pack k-point grid was used to ensure the accuracy of vibrational frequencies. The thermal contributions to the Gibbs free energy were calculated at 298.15 K.

Under acidic conditions, the overall HER can be expressed as:

$$2H^{+} + 2e^{-} \rightarrow H_{2}$$
 (1)

In the Volmer–Heyrovsky mechanism, it proceeds through two primary steps, the adsorption of an H atom onto the catalyst surface and a desorption process where another H atom combines with the adsorbed H atom to form molecular hydrogen:

$$H^+ + e^- + * \to H^*$$
 (2)

$$H^+ + e^- + H^* \to H_2$$
 (3)

where * represents an active site and H* indicates a hydrogen atom adsorbed on the catalyst surface. The structural optimizations and the corresponding ZPE corrections for H-adsorbed borophenes are performed using the same computational parameters and workflow as described above. The free energy of hydrogen adsorption ($\Delta G_{\rm H}$) is widely regarded as a key descriptor for evaluating the catalytic performance of HER [69], which is given by:

$$\Delta G_{\mathrm{H}^*} = \Delta E_{\mathrm{H}} + \Delta E_{\mathrm{ZPE}} - T \Delta S_{\mathrm{H}} \tag{4}$$

$$\Delta E_{\rm H} = E_{n{\rm H}^*} - E_{(n-1){\rm H}^*} - \frac{1}{2} E_{{\rm H}_2}$$
 (5)

where $\Delta E_{\rm H}$ is the change in electronic energy due to hydrogen adsorption, $\Delta E_{\rm ZPE}$ represents the change in zero-point energy, T is the temperature, and $\Delta S_{\rm H}$ denotes the change in entropy of the hydrogen atom during adsorption. $E_{n{\rm H}^*}$ and $E_{{\rm H}_2}$ are the electronic energy of the system with n adsorbed H atoms and hydrogen molecule, respectively. We first focused on the freestanding borophene sheets, and subsequently constructed borophene/Ag(111) heterostructures to simulate realistic substrate-supported systems.

RESULTS AND DISCUSSION

To establish a comprehensive understanding of the intrinsic properties of borophene, we began our investigation with freestanding monolayer structures, avoiding the influence of external perturbations such as substrates or dopants. It enabled us to examine the fundamental electronic structure and catalytic characteristics of borophene in its pristine state. In particular, we systematically explored the HER performance by evaluating the hydrogen adsorption behavior at various adsorption sites on four borophene phases: α , β 12, γ 3, and trigonal. These structures were chosen based on their distinct bonding motifs and stability profiles as reported in previous studies. Considering that most borophene structures are experimentally synthesized on metallic substrates, we investigated the influence of metal support on their catalytic performance. In this work, an Ag(111) surface was selected as a representative substrate, given its frequent use in the epitaxial growth of borophene. By comparing the energetics and electronic structures of borophene before and after substrate introduction, we systematically evaluated the impact of substrate effects on its catalytic behavior.

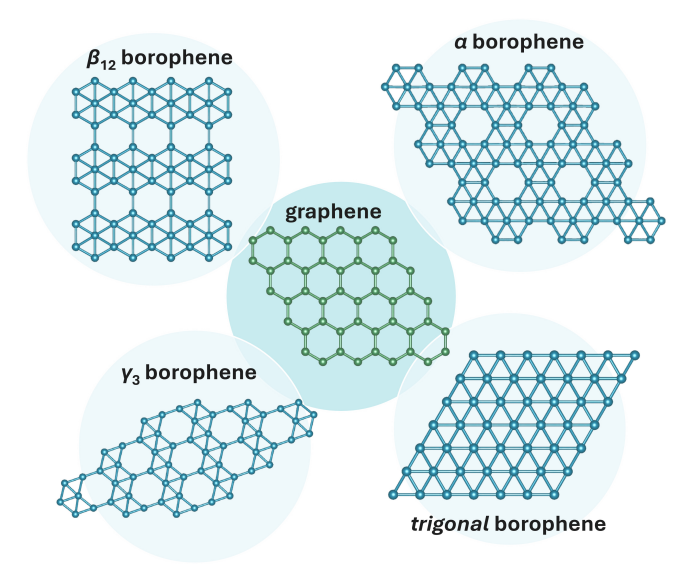


FIG. 1. Geometric configurations of graphene (center panel) and four free-standing borophenes. The structures shown from left to right and top to bottom correspond to the β_{12} , α , γ_3 , and trigonal phases, respectively.

Structure and stability of freestanding surface

Four freestanding borophene surfaces are taken as examples. The trigonal borophene is a two-dimensional planar lattice composed entirely of triangular motifs. α , β_{12} , and γ_3 phases are formed by introducing vacancies at specific positions within the trigonal surface. Compared to the hexagonal lattice of graphene, these borophenes have additional atoms in the centers of the vacant hexagons. Notably, the latter three phases have already been successfully synthesized in experiments [46, 47, 49]. Fig. 1 shows the four borophene configurations. Due to the distinct atomic arrangements, the bonding environments in these four phases differ significantly. For instance, the trigonal phase consists entirely of fully coordinated boron atoms, whereas the α phase contains 5-fold coordinated boron atoms due to the presence of vacancies. In contrast, the $\gamma 3$ phase includes only 3- and 4-fold coordinated boron atoms. The β_{12} phase contains all the above bonding types. These bonding variations strongly suggest that also the HER performance of these different phases might be distinct. To model the adsorption configurations and ensure negligible periodic interactions between adsorbates, different sufficiently large supercell sizes were used for each phase: a $2 \times 2 \times 1$ supercell for the α phase, $3 \times 2 \times 1$ for the β_{12} phase, $3 \times$ 3×1 for the γ_3 phase, and $2 \times 2 \times 1$ for the trigonal phase. Remarkably, these structural modifications preserve the overall planar geometry of surfaces with respect to perpendicular relaxations. To examine the stability of the planar structure, we applied various arbitrary distortions along the out-of-plane direction.

TABLE I. Average B-B bond length of the four borophene phases. The notation "bl(m-n)" refers to the length of a B-B bond formed between m-fold coordinated and n-fold coordinated boron atoms. Unit of each value is Å.

phases	bl(4-4)	bl(4-5)	bl(4-6)	bl(5-5)	bl(5-6)	bl(6-6)
α	_	_	_	1.671	1.687	
β_{12}	1.644	1.678	1.711	1.753	1.700	
γ_3	1.611	1.691	_	1.638	_	_
trigonal	_	_	_	_	_	1.704

scenarios, the systems relaxed back to nearly perfect planar configurations, indicating the intrinsic robustness of the 2-dimensional geometry. The lengths of the boron bonds range from 1.63 Å to 1.75 Å. Detailed information about each lattice is provided in Table I. To evaluate the relative thermodynamic stability of the four borophene phases, we compared their formation energy per unit area. This analysis yields that the trigonal phase exhibits the lowest energy per unit area with the value of -2.443 eV/Ų. The α phase has a slightly higher energy (-2.338 eV/Ų). The energy per unit area of the β phase is -2.157 eV/Ų. The γ_3 phase with a formation energy per unit area of -2.096 eV/Ų is the energetically least favorable structure among the considered phases.

HER performance of freestanding borophenes

To better understand the interaction between hydrogen and various phases, potential energy surfaces (PES) are first mapped on the monolayer borophene with a single H atom adsorbed. Considering surface symmetry and periodicity, the H atom is moved within a specific region on each surface, which consists of two adjacent triangular units [highlighted in yellow This area includes both high- and in Fig. 2 (a)]. low-coordination sites, thereby capturing the essential electronic features of the entire surface. The vertical distance between H and borophene is determined by scanning the total energy as a function of height. The distance corresponding to the minimum energy is chosen and fixed in the subsequent PES evaluations. For α , β_{12} , γ_3 , and , the H-borophene distances are fixed as 1.710 Å, 1.712 Å, 1.690 Å, and 1.760 Å, respectively. We evenly selected 100×100 sampling points within the aforementioned surface region. The single-point energy at each sampling point is calculated using the computational parameters mentioned in the previous section (the boron atoms are frozen here). The lowest energy of each phase is taken as the reference. The resulting PES maps are shown in Figs. 2 (b-e). It reveals that areas near lower-coordinated on-top adsorption sites exhibit lower potential energy, such as the 5-fold site on α , the 4-fold site on both β_{12} and γ_3 . Notably, for the trigonal phase, composed entirely of saturated boron

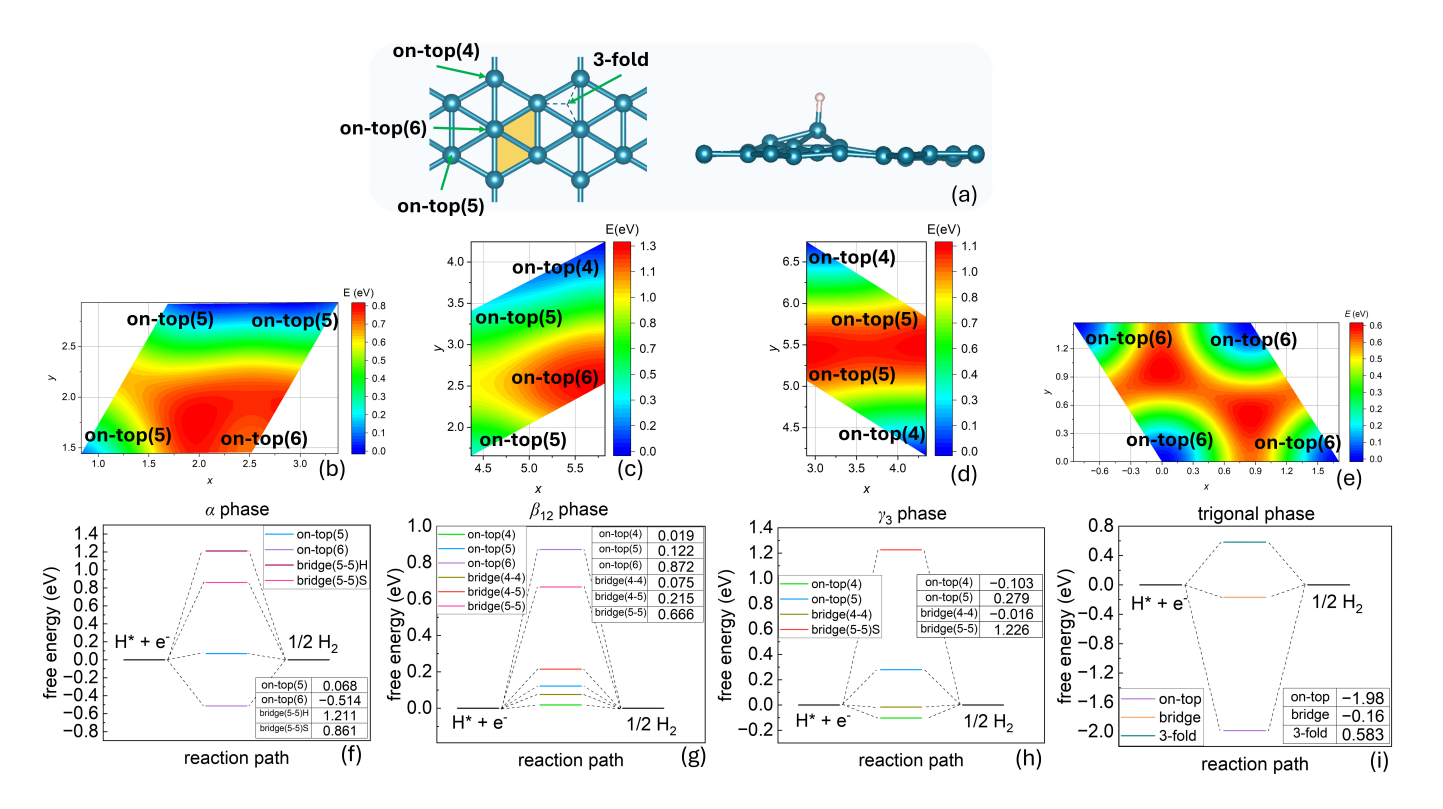


FIG. 2. (a) The left panel illustrates representative adsorption sites on borophene, including on-top(n) and 3-fold sites, where n=4, 5, or 6 denotes the coordination number of the underlying boron atom (i.e., 4-fold, 5-fold, and 6-fold coordinated sites, respectively). The right panel schematically shows the out-of-plane distortion of the borophene surface upon hydrogen adsorption. Panels (b-e) depict the potential energy surface of single-H adsorption of the four boronphene phases: (b) α , (c) β_{12} , (d) γ_3 , and (e) trigonal. The H atom is moved within a specific region consists of two adjacent triangular units as highlighted in panel (a). The distances between H and boron surface are fixed as 1.710 Å, 1.712 Å, 1.690 Å, and 1.760 Å on the α , β_{12} , γ_3 , and trigonal phases, respectively. The corresponding on-top site types at each vertex are also labeled in each panel. Panels (f-i) depict the free energy diagrams for hydrogen adsorption on the α , β_{12} , γ_3 , and trigonal phases, respectively. Each panel includes a table listing the calculated hydrogen adsorption free energy (ΔG_{H^*}) for the corresponding adsorption sites. In the table, "bridge(m-n)" denotes a bridge site located between two adjacent boron atoms with m- and n-fold coordination. The signs "bridge(5-5)H" and "bridge(5-5)S" in panel (b) refer to bridge sites located along the edges of hollow hexagons and hexagons containing an additional boron atom at the center, respectively.

atoms, all on-top sites show identical potential energies that are lower than those at other adsorption sites, such as bridge and hollow sites. This suggests that hydrogen atoms preferentially adsorb at undercoordinated boron sites, where stronger interactions are expected.

Here, the HER mechanism is described by the Volmer–Heyrovsky pathway, as shown in Eqs. 2 and 3. Combined with the PES results and geometric features of the four phases, we select representative adsorption sites, including on-top, bridge, and three-fold hollow sites, to evaluate their hydrogen evolution performance. These sites span different coordination environments and reflect the electronic diversity of each surface. In order to distinguish them, we assign labels based on their local coordination environment. Specifically, on-top sites located on 4-fold, 5-fold, and 6-fold coordinated boron atoms are labeled as on-top(4), on-top(5), and on-top(6), respectively. Bridge sites are denoted as "bridge(m-n)", where m and n are the coordination numbers of adjacent

atoms. 3-fold site is located in the center of the triangle motif [shown in Fig. 2 (a)]. For the trigonal phase, which exhibits a uniform arrangement of saturated boron atoms, only one unique site exists for each type, and no further distinction is necessary. The Gibbs free energy of hydrogen adsorption (ΔG_{H^*}) is utilized as a criterion to quantify the catalytic activity. Efficient HER catalysts require a good balance between hydrogen adsorption and desorption (hydrogen binds neither too weakly nor too strongly); hence, the reaction is considered optimal when the value of ΔG_{H^*} is close to zero [70]. We optimized each borophene surface again with a single hydrogen atom adsorbed by using the same computational conditions as for the pristine structures. Local structural distortions are observed around the adsorption sites after relaxation, due to the release of adsorption-induced strain. Notably, the hydrogen atoms initially adsorbed at three-fold sites tend to migrate to nearby on-top or bridge positions, indicating a more confined distribution of energetically

favorable adsorption sites. The free energy diagrams of HER on the four borophene phases are depicted in Figs. 2 (f-i).

In general, an on-top site located on the low-coordination boron atom exhibits the optimal adsorption free energies. For example, the on-top(4) site (located on a 4-fold coordinated boron atom) on β_{12} yields the lowest value of 0.019 eV in this phase. As the coordination number increases, the value of ΔG_{H^*} also rises. For instance, the on-top(5) site on the β_{12} phase exhibits a moderate adsorption free energy of 0.122 eV, while the on-top(6) site shows a much higher value of 0.872 eV, indicating reduced HER activity. Similar results can be found in both α and γ_3 phases. This trend is consistent with our previous analysis based on the PES images, where low-coordination sites generally present deeper potential wells. noteworthy that certain bridge sites, especially those spanning lower-coordinated atoms, also yield ΔG_{H^*} values comparable to on-top sites. On the γ_3 surface, the bridge(4-4) site exhibits a remarkably low value of -0.016 eV, which is the lowest value among all the selected sites on four phases. In contrast, the bridge (5-5) site shows a much higher value of 1.226 eV. As for the α phase, both bridge sites span two 5-fold coordinated boron atoms. However, the one located at the edge of a hollow hexagon "bridge(5-5)H" exhibits a noticeably higher adsorption free energy compared to the one between two filled hexagons "bridge(5-5)S". values can be found on the bridge(5-5)H site of β_{12} (0.666 eV) and the bridge(5-5)S site of γ_3 (1.226 eV). This can be attributed to the lower local charge density in this region, which weakens the interaction between the boron atoms and the adsorbed hydrogen. Specifically, the trigonal structure exhibits a distinct behavior. The on-top site shows a significantly negative adsorption free energy of -1.980 eV, suggesting overly strong hydrogen binding that hinders desorption and thus reduces HER efficiency. Meanwhile, the bridge and three-fold sites also yield slightly higher values of -0.160 and 0.583eV, respectively. We attribute this deviation to the fully saturated coordination environment in the trigonal lattice, which lacks the local geometric or electronic asymmetry typically found near low-coordinated sites. These results suggest that the α , β_{12} , and γ_3 phases hold great promise for HER catalysis, whereas the trigonal phase is comparatively less effective.

Structures and stabilities of borophenes on silver substrate

The calculations on the freestanding borophenes offer fundamental understanding of HER properties, while practical applications often involve interactions with supporting substrates. Considering that lots of borophene phases are experimentally synthesized on silver substrates [38, 43, 71], we utilize an Ag(111)surface to investigate how substrate interactions affect the structural and electronic properties of these systems. Each of the four aforementioned borophenes is placed on a three-layer Ag(111) slab with a lattice mismatch below 5%. The heterostructures are then geometrically optimized using the same computational parameters as for the freestanding borophenes. During the relaxation, the bottom two layers of the silver substrate are fixed to simulate bulk constraints, while the topmost layer in direct contact with borophene is allowed to fully relax. The resulting relaxed structures are shown in Fig. 3. The optimized vertical distances between the Ag(111) surface and the α , β_{12} , γ_3 , and trigonal borophenes are 2.912 Å, 2.410 Å, 2.211 Å, and 3.123 Å, respectively. The presence of the Ag substrate induces out-of-plane distortions in all cases. In particular, the trigonal structure undergoes significant reconstruction, which is not due to its highly saturated bonding environment of its boron atoms but rather to its densely packed bonding environment. Unlike boron configurations with vacancies, which can locally adjust to release strain, the close-packed nature of the trigonal structure offers limited geometric flexibility, leading to substantial reconstruction under stress.

To quantify the interfacial interaction strength across different borophene phases, we compute the bonding energy per unit area (E_{bond}) as:

$$E_{\text{bond}} = \frac{E_{\text{borophene/Ag}} - E_{\text{Ag}} - E_{\text{borophene}}}{A}$$
 (6)

where $E_{\rm borophene/Ag}$ is the total energy of the borophene/Ag(111) heterostructure, $E_{\rm Ag}$ is the total energy of the clean Ag slab, $E_{\text{borophene}}$ is the energy of the freestanding borophene layer with the same lattice size as in the heterostructure, and A is the interfacial area. The bonding energies for the four phases are -0.167 eV/Å^2 (α) , $-0.201 \text{ eV/Å}^2(\beta_{12})$, $-0.188 \text{ eV/Å}^2(\gamma_3)$, and -0.204eV/Å² (trigonal), respectively. Among the four phases, the trigonal borophene exhibits the strongest interaction with the silver substrate, followed closely by β_{12} and γ_3 , while the α phase shows the weakest interfacial bonding. In particular, the trigonal borophene initially features a highly saturated bonding environment around its boron atoms. Upon interaction with the Ag(111) substrate, it undergoes significant out-of-plane distortions, which help release internal stress within the borophene layer. These distortions also bring certain boron atoms closer to the silver surface (around 1.78 Å), thereby enhancing orbital overlap and strengthening the interfacial interaction.

To evaluate the thermodynamic stability of supported borophene structures, we calculate the formation energy per boron atom using the following expression [72, 73]:

$$E_{\text{form}} = \frac{E_{\text{borophene/Ag}} - E_{\text{Ag}} - N \times \mu_{\text{B}}}{A}$$
 (7)

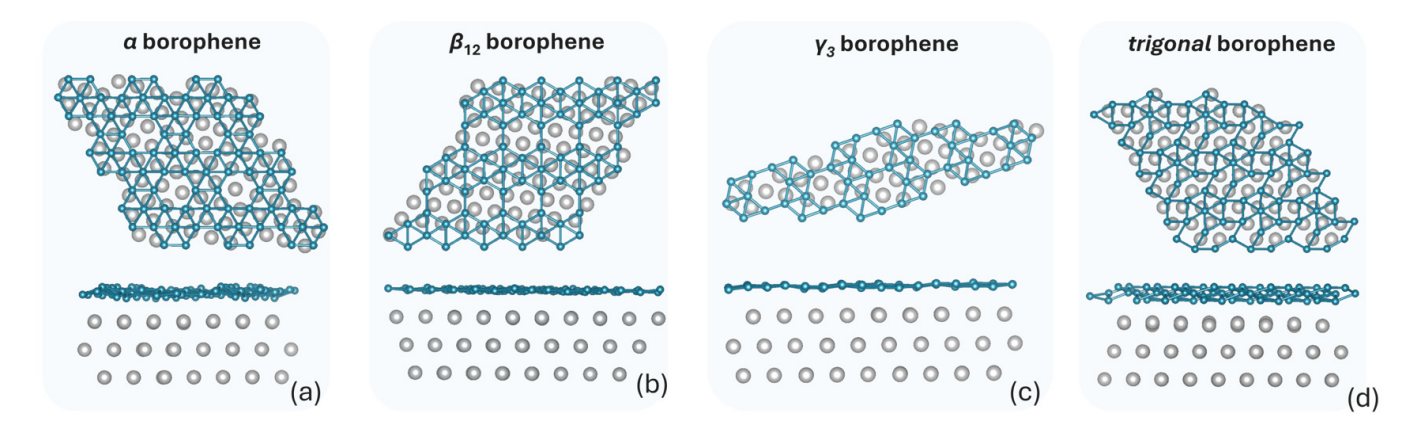


FIG. 3. Optimized structures of borophene phases on the Ag(111) substrate: (a) α , (b) β_{12} , (c) γ_3 , and (d) trigonal phases. For each configuration, the upper panel shows the top view and the lower panel displays the side view, highlighting the interfacial interaction and structural deformation upon adsorption.

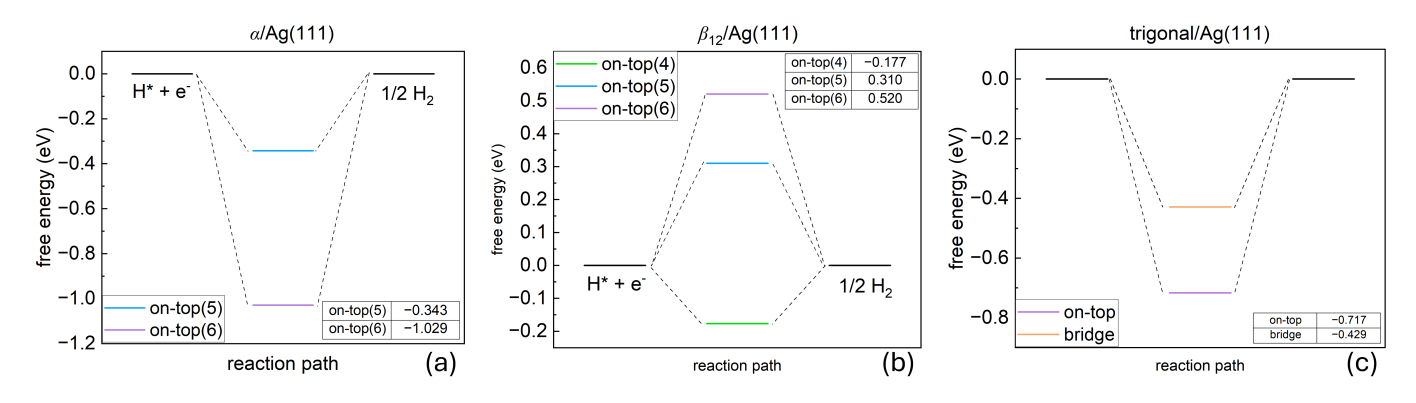


FIG. 4. Hydrogen adsorption free energy diagrams for (a) α , (b) β_{12} , and (c) trigonal borophene phases on the Ag(111) substrate. Each panel shows the calculated ΔG_{H^*} values at different adsorption sites, indicating the variation in hydrogen adsorption behavior across different borophene/Ag(111) interfaces.

TABLE II. Summary of structural and electronic properties of borophene/Ag(111) heterostructures. d denotes the vertical distance between the borophene layer and Ag(111) surface; $E_{\rm bond}$ denotes average interfacial bonding energy per unit area; $E_{\rm form}$ is the formation energy per boron atom; Φ denotes the work function of the heterostructure. Values in parentheses indicate the work function of the corresponding pristine borophene sheets.

phases	d (Å)	$E_{\rm bond}$	$E_{ m form}$	Φ (eV)
		$(eV/Å^2)$	$(eV/Å^2)$	
α/Ag	2.912	-0.167	-0.164	4.342 (3.986)
β_{12}/Ag	2.410	-0.201	-0.202	4.344(4.793)
$\gamma_3/{ m Ag}$	2.211	-0.188	-0.181	4.279(4.681)
$\frac{\rm trigonal/Ag}$	3.123	-0.204	-0.283	4.747 (3.098)

where $\mu_{\rm B}$ is the chemical potential of a single boron atom, typically taken from the energy per atom in the corresponding pristine borophene phases. Interestingly, the lowest $E_{\rm form}$ is found on the trigonal phase with a negative value of $-0.283~{\rm eV/\mathring{A}^2}$, suggesting it is the

most stable configuration on the Ag(111) surface. The β_{12} and γ_3 phases also show relatively high stability, consistent with their moderate interface bonding energies and preserved lattice structures. The α phase, which has the stablest pristine configuration, has the highest formation energy (-0.164 eV/Å²), indicating weaker overall thermodynamic favorability, consistent with its weaker bonding interaction with the Ag(111) surface.

HER performance of supported borophenes

Now we focus on the HER performance of the supported borophenes. The geometric optimizations for the heterostructures with a single H atom adsorbed on the borophene surface are performed. The initial adsorption sites are chosen in accordance with those selected in the freestanding scenarios. After relaxation, noticeable differences occur: in both the α and β_{12} structures, all the hydrogen atoms eventually relax to on-top sites. For the trigonal structure, both on-top and

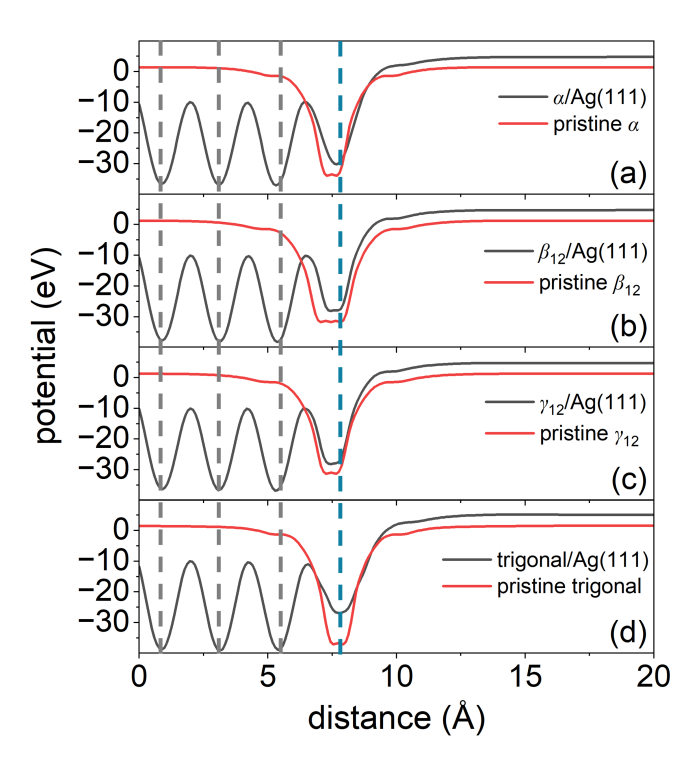


FIG. 5. Plane-averaged electrostatic potential along the z-direction of borophene phases on the Ag(111) substrate: (a) $\alpha/{\rm Ag}(111)$, (b) $\beta_{12}/{\rm Ag}(111)$, (c) $\gamma_3/{\rm Ag}(111)$, and (d) trigonal/Ag(111). The red and black lines denote the potential of the borophene/Ag and pristine borophene structures, respectively. The dashed lines from left to right denote the positions of silver and boron layers.

bridge sites remain stable after optimization, while the H atom initially located at the 3-fold site relaxes to an on-top site. As for the γ_3 phase, it undergoes significant structural disruption upon hydrogen adsorption, leading to a complete breakdown of its planar geometry, and is therefore excluded from the subsequent analysis. This indicates that it is in general not appropriate to transfer properties of free-standing layers to those of supported layers.

The corresponding Gibbs free energies for hydrogen adsorption on the supported α , β_{12} , and trigonal borophene structures are summarized in Fig. 4. In the freestanding case, sites with lower coordination tend to exhibit superior HER activity. This feature is preserved in the silver-supported structures. On the β_{12} phase, the most active site is the on-top(4) site with the lowest relative ΔG_{H^*} of -0.177 eV. For α , the most favorable one is the on-top(5) site ($\Delta G_{H^*} = 0.310$ eV), which exhibits similar activity to the on-top(5) site of β_{12} ($\Delta G_{H^*} = 0.343$ eV). Importantly, compared to their pristine counterparts, the absolute values of ΔG_{H^*} are increased in both α and β_{12} , indicating a reduced HER performance upon substrate support. A work function analysis is applied to evaluate the influence of the silver substrate support on the electronic

properties of borophene. For the α phase, as shown in Table II, the work function increases significantly from 3.986 eV to 4.342 eV upon interaction with the Ag(111) substrate. In contrast, the β_{12} phase exhibits a moderate decrease of 0.449 eV, resulting in a final value of 4.344 eV, which is comparable to that of the supported α phase. These changes can be attributed to the charge redistribution induced by the out-of-plane distortions of the boron surfaces upon adsorption. As shown in Fig. 5, within the borophene region, the electrostatic potential increases from approximately -32 eV in the freestanding structures to around -29 eV upon adsorption on the Ag(111) surface. Correspondingly, the vacuum level shifts from about 1.3 eV to 4.3 eV. The upward shift in both internal and vacuum potentials reveals the influence of substrate-induced charge redistribution and dipole formation at the borophene-silver interface. In particular, the α structure undergoes a larger out-of-plane distortion than the β_{12} phase, leading to a more substantial modification of its surface electronic environment and hence a greater shift in work function. A similar result of limited work-function change can also be found in the γ_3 phase.

Nevertheless, in the trigonal structure, the bridge site exhibits a lower absolute value of ΔG_{H^*} compared to that on the freestanding surface [Fig. 4 (c)]. In addition, similar to the α phase, it exhibits the largest increase in work function (from 3.098 eV to 4.747 eV) due to the substantial geometric distortion, and the hydrogen adsorption free energy becomes negative upon substrate interaction. An interesting correlation is observed between the variation in work function and the adsorption free energy of hydrogen. It indicates that an increase in work function facilitates electron transfer from the substrate to the adsorbed hydrogen, thereby stabilizing the H* intermediate. In other words, surfaces with increased work functions tend to favor electron donation to hydrogen. Eventually, such a trend increases the HER performance on the bridge site of the trigonal phase, but reduces the HER performance on the on-top sites of α and β_{12} phases.

CONCLUSION

In this work, we systematically studied the HER performance of four borophene phases using first-principles calculations, including α , γ_3 , β_{12} , and trigonal phases. We found that in the freestanding monolayer surfaces, low-coordinated boron sites generally exhibit more favorable hydrogen adsorption, with the α , β_{12} , and γ_3 phases showing promising catalytic performance. In contrast, the trigonal phase performs poorly due to its highly coordinated, saturated bonding environment. When supported on an Ag(111) surface, the borophene structures undergo substrate-induced distortions, which tend to reduce HER activity by weakening adsorption strength. Although the coordination-dependent trend is largely preserved and some sites on the supported layers still exhibit moderate activity, this result clearly indicates that a metal support can have a significant influence on the properties of two-dimensional layers. These findings clarify the crucial role of local atomic coordination in governing hydrogen adsorption energetics and HER catalytic activity in borophene. Moreover, the study highlights the significant impact of substrate interactions, which can both modulate structural stability and electronic properties, thereby influencing catalytic behavior. Understanding these effects provides valuable insight for the rational design and optimization of boron-based catalysts.

ACKNOWLEDGMENTS

Financial Support by the German Federal Ministry of Economic Affairs and Climate Action through the AQUAS project (01MQ22003C) and the Dr. Barbara Mez-Starck Foundation are gratefully acknowledged.

- * jing-1.liu@uni-ulm.de † axel.gross@uni-ulm.de
- D. Deng, K. Novoselov, Q. Fu, N. Zheng, Z. Tian, and X. Bao, Catalysis with two-dimensional materials and their heterostructures, Nat. Nanotechnol. 11, 218 (2016).
- [2] L. Tang, X. Meng, D. Deng, and X. Bao, Confinement catalysis with 2D materials for energy conversion, Adv. Mater. 31, 1901996 (2019).
- [3] L. Zhao, B. Wang, and R. Wang, A critical review on new and efficient 2D materials for catalysis, Adv. Mater. Interfaces 9, 2200771 (2022).
- [4] A. K. Katiyar, A. T. Hoang, D. Xu, J. Hong, B. J. Kim, S. Ji, and J.-H. Ahn, 2D materials in flexible electronics: recent advances and future prospectives, Chem. Rev. 124, 318 (2023).
- [5] E. C. Ahn, 2D materials for spintronic devices, npj 2D Mater. Appl. 4, 17 (2020).
- [6] A. Groß, Adsorption at nanostructured surfaces from first principles, J. Comput. Theor. Nanosci. 5, 894 (2008).
- [7] J. López-Andarias, A. Bauzá, N. Sakai, A. Frontera, and S. Matile, Remote control of anion-π catalysis on fullerene-centered catalytic triads, Angew. Chem. Int. Ed. 130, 11049 (2018).
- [8] Y. Pan, X. Liu, W. Zhang, Z. Liu, G. Zeng, B. Shao, Q. Liang, Q. He, X. Yuan, D. Huang, et al., Advances in photocatalysis based on fullerene C₆₀ and its derivatives: Properties, mechanism, synthesis, and applications, Appl. Catal. B 265, 118579 (2020).
- [9] S. J. Hong, H. Chun, M. Hong, and B. Han, Nand B-doped fullerene as peroxidase-and catalase-like metal-free nanozymes with pH-switchable catalytic

- activity: A first-principles approach, Appl. Surf. Sci. **598**, 153715 (2022).
- [10] X. Chang, Y. Xu, and M. von Delius, Recent advances in supramolecular fullerene chemistry, Chem. Soc. Rev. 53, 47 (2024).
- [11] A. S. Brady-Estevez, S. Kang, and M. Elimelech, Carbon nanotubes, Small 4, 481 (2008).
- [12] P. Serp and E. Castillejos, Catalysis in carbon nanotubes, ChemCatChem 2, 41 (2010).
- [13] M. F. De Volder, S. H. Tawfick, R. H. Baughman, and A. J. Hart, Carbon nanotubes: present and future commercial applications, Science 339, 535 (2013).
- [14] A. K. Geim, Graphene: Status and prospects, Science 324, 1530 (2009).
- [15] Y. Li, H. Wang, L. Xie, Y. Liang, G. Hong, and H. Dai, MoS₂ nanoparticles grown on graphene: An advanced catalyst for the hydrogen evolution reaction, J. Am. Chem. Soc. 133, 7296 (2011).
- [16] H.-J. Qiu, Y. Ito, W. Cong, Y. Tan, P. Liu, A. Hirata, T. Fujita, Z. Tang, and M. Chen, Nanoporous graphene with single-atom nickel dopants: An efficient and stable catalyst for electrochemical hydrogen production, Angew. Chem. Int. Ed. 54, 14031 (2015).
- [17] Y. Jiao, Y. Zheng, K. Davey, and S.-Z. Qiao, Activity origin and catalyst design principles for electrocatalytic hydrogen evolution on heteroatom-doped graphene, Nat. Energy 1, 1 (2016).
- [18] X. Li, J. Yu, S. Wageh, A. A. Al-Ghamdi, and J. Xie, Graphene in photocatalysis: a review, Small 12, 6640 (2016).
- [19] C. Lee, X. Wei, J. W. Kysar, and J. Hone, Measurement of the elastic properties and intrinsic strength of monolayer graphene, Science 321, 385 (2008).
- [20] A. H. Castro Neto, F. Guinea, N. M. R. Peres, K. S. Novoselov, and A. K. Geim, The electronic properties of graphene, Rev. Mod. Phys. 81, 109 (2009).
- [21] C. Soldano, A. Mahmood, and E. Dujardin, Production, properties and potential of graphene, Carbon 48, 2127 (2010).
- [22] A. Olabi, M. A. Abdelkareem, T. Wilberforce, and E. T. Sayed, Application of graphene in energy storage device a review, Renewable Sustainable Energy Rev. 135, 110026 (2021).
- [23] Y. Qi, L. Sun, and Z. Liu, Super graphene-skinned materials: An innovative strategy toward graphene applications, ACS Nano 18, 4617 (2024).
- [24] H. Gao, Z. Wang, J. Cao, Y. C. Lin, and X. Ling, Advancing nanoelectronics applications: Progress in non-van der waals 2D materials, ACS Nano 18, 16343 (2024).
- [25] J. Zhao, P. Ji, Y. Li, R. Li, K. Zhang, H. Tian, K. Yu, B. Bian, L. Hao, X. Xiao, et al., Ultrahigh-mobility semiconducting epitaxial graphene on silicon carbide, Nature 625, 60 (2024).
- [26] J. Azizi, A. Groß, and H. Euchner, Computational investigation of carbon based anode materials for liand post-li- ion batteries, ChemSusChem 17, e202301493 (2024).
- [27] H.-J. Zhai, B. Kiran, J. Li, and L.-S. Wang, Hydrocarbon analogues of boron clusters—planarity, aromaticity and antiaromaticity, Nat. Mater. 2, 827 (2003).
- [28] N. Gonzalez Szwacki, A. Sadrzadeh, and B. I. Yakobson, B₈₀ fullerene: An ab initio prediction of geometry, stability, and electronic structure, Phys. Rev. Lett. 98,

- 166804 (2007).
- [29] W. Huang, A. P. Sergeeva, H.-J. Zhai, B. B. Averkiev, L.-S. Wang, and A. I. Boldyrev, A concentric planar doubly π-aromatic B⁻₁₉ cluster, Nat. Chem. 2, 202 (2010).
- [30] H.-J. Zhai, Y.-F. Zhao, W.-L. Li, Q. Chen, H. Bai, H.-S. Hu, Z. A. Piazza, W.-J. Tian, H.-G. Lu, Y.-B. Wu, Y.-W. Mu, G.-F. Wei, Z.-P. Liu, J. Li, S.-D. Li, and L.-S. Wang, Observation of an all-boron fullerene, Nat. Chem. 6, 727 (2014).
- [31] B. Kiran, S. Bulusu, H.-J. Zhai, S. Yoo, X. C. Zeng, and L.-S. Wang, Planar-to-tubular structural transition in boron clusters: B₂₀ as the embryo of single-walled boron nanotubes, Proc. Natl. Acad. Sci. 102, 961 (2005).
- [32] K. C. Lau, R. Orlando, and R. Pandey, First-principles study of crystalline bundles of single-walled boron nanotubes with small diameter, J. Physics: Condens. Matter 20, 125202 (2008).
- [33] F. Liu, C. Shen, Z. Su, X. Ding, S. Deng, J. Chen, N. Xu, and H. Gao, Metal-like single crystalline boron nanotubes: synthesis and in situ study on electric transport and field emission properties, J. Mater. Chem. 20, 2197 (2010).
- [34] X. Wu, J. Dai, Y. Zhao, Z. Zhuo, J. Yang, and X. C. Zeng, Two-dimensional boron monolayer sheets, ACS Nano 6, 7443 (2012).
- [35] B. Feng, J. Zhang, Q. Zhong, W. Li, S. Li, H. Li, P. Cheng, S. Meng, L. Chen, and K. Wu, Experimental realization of two-dimensional boron sheets, Nat. Chem. 8, 563 (2016).
- [36] Z. Wu, G. Tai, W. Shao, R. Wang, and C. Hou, Experimental realization of quasicubic boron sheets, Nanoscale 12, 3787 (2020).
- [37] Z. A. Piazza, H.-S. Hu, W.-L. Li, Y.-F. Zhao, J. Li, and L.-S. Wang, Planar hexagonal B₃₆ as a potential basis for extended single-atom layer boron sheets, Nat. Comm. 5, 3113 (2014).
- [38] D. Li, J. Gao, P. Cheng, J. He, Y. Yin, Y. Hu, L. Chen, Y. Cheng, and J. Zhao, 2D boron sheets: Structure, growth, and electronic and thermal transport properties, Adv. Funct. Mater. 30, 1904349 (2020).
- [39] B. Kiraly, X. Liu, L. Wang, Z. Zhang, A. J. Mannix, B. L. Fisher, B. I. Yakobson, M. C. Hersam, and N. P. Guisinger, Borophene synthesis on Au(111), ACS Nano 13, 3816 (2019).
- [40] W. Li, L. Kong, C. Chen, J. Gou, S. Sheng, W. Zhang, H. Li, L. Chen, P. Cheng, and K. Wu, Experimental realization of honeycomb borophene, Sci. Bull. 63, 282 (2018).
- [41] R. Wu, I. K. Drozdov, S. Eltinge, P. Zahl, S. Ismail-Beigi, I. Božović, and A. Gozar, Large-area single-crystal sheets of borophene on Cu(111) surfaces, Nat. Nanotechnol. 14, 44 (2019).
- [42] J.-Y. Chung, Y. Yuan, T. P. Mishra, C. Joseph, P. Canepa, P. Ranjan, E. H. S. Sadki, S. Gradečak, and S. Garaj, Structure and exfoliation mechanism of two-dimensional boron nanosheets, Nat. Comm. 15, 6122 (2024).
- [43] Q. Zhong, L. Kong, J. Gou, W. Li, S. Sheng, S. Yang, P. Cheng, H. Li, K. Wu, and L. Chen, Synthesis of borophene nanoribbons on Ag(110) surface, Phys. Rev. Mater. 1, 021001 (2017).
- [44] B. Feng, O. Sugino, R.-Y. Liu, J. Zhang, R. Yukawa, M. Kawamura, T. Iimori, H. Kim, Y. Hasegawa, H. Li, L. Chen, K. Wu, H. Kumigashira, F. Komori, T.-C.

- Chiang, S. Meng, and I. Matsuda, Dirac fermions in borophene, Phys. Rev. Lett. **118**, 096401 (2017).
- [45] X. Liu, Z. Wei, I. Balla, A. J. Mannix, N. P. Guisinger, E. Luijten, and M. C. Hersam, Self-assembly of electronically abrupt borophene/organic lateral heterostructures, Sci. Adv. 3, e1602356 (2017).
- [46] X. Liu, Z. Zhang, L. Wang, B. I. Yakobson, and M. C. Hersam, Intermixing and periodic self-assembly of borophene line defects, Nat. Mater. 17, 783 (2018).
- [47] X. Liu and M. C. Hersam, Borophene-graphene heterostructures, Sci. Adv. 5, eaax6444 (2019).
- [48] N. A. Vinogradov, A. Lyalin, T. Taketsugu, A. S. Vinogradov, and A. Preobrajenski, Single-phase borophene on Ir(111): Formation, structure, and decoupling from the support, ACS Nano 13, 14511 (2019).
- [49] Y. Wang, L. Kong, C. Chen, P. Cheng, B. Feng, K. Wu, and L. Chen, Realization of regular-mixed quasi-1D borophene chains with long-range order, Adv. Mater. 32, 2005128 (2020).
- [50] X.-F. Zhou, X. Dong, A. R. Oganov, Q. Zhu, Y. Tian, and H.-T. Wang, Semimetallic two-dimensional boron allotrope with massless dirac fermions, Phys. Rev. Lett. 112, 085502 (2014).
- [51] B. Feng, J. Zhang, R.-Y. Liu, T. Iimori, C. Lian, H. Li, L. Chen, K. Wu, S. Meng, F. Komori, and I. Matsuda, Direct evidence of metallic bands in a monolayer boron sheet, Phys. Rev. B 94, 041408 (2016).
- [52] L. Adamska, S. Sadasivam, J. J. I. Foley, P. Darancet, and S. Sharifzadeh, First-principles investigation of borophene as a monolayer transparent conductor, J. Phys. Chem. C 122, 4037 (2018).
- [53] Y. An, J. Jiao, Y. Hou, H. Wang, D. Wu, T. Wang, Z. Fu, G. Xu, and R. Wu, How does the electric current propagate through fully-hydrogenated borophene?, Phys. Chem. Chem. Phys. 20, 21552 (2018).
- [54] S. H. Mir, S. Chakraborty, P. C. Jha, J. Wärnå, H. Soni, P. K. Jha, and R. Ahuja, Two-dimensional boron: Lightest catalyst for hydrogen and oxygen evolution reaction, Appl. Phys. Lett. 109, 053903 (2016).
- [55] Y. Chen, G. Yu, W. Chen, Y. Liu, G.-D. Li, P. Zhu, Q. Tao, Q. Li, J. Liu, X. Shen, H. Li, X. Huang, D. Wang, T. Asefa, and X. Zou, Highly active, nonprecious electrocatalyst comprising borophene subunits for the hydrogen evolution reaction, J. Am. Chem. Soc. 139, 12370 (2017).
- [56] L. Shi, C. Ling, Y. Ouyang, and J. Wang, High intrinsic catalytic activity of two-dimensional boron monolayers for the hydrogen evolution reaction, Nanoscale 9, 533 (2017).
- [57] Y. Singh, S. Back, and Y. Jung, Computational exploration of borophane-supported single transition metal atoms as potential oxygen reduction and evolution electrocatalysts, Phys. Chem. Chem. Phys. 20, 21095 (2018).
- [58] M. Xu, R. Wang, K. Bian, C. Hou, Y. Wu, and G. Tai, Triclinic boron nanosheets high-efficient electrocatalysts for water splitting, Nanotechnol. 33, 075601 (2021).
- [59] X. Wang, R. Wu, P. Tian, Y. Yan, Y. Gao, and F. Xuan, Borophene nanoribbons via strain engineering for the hydrogen evolution reaction: A first-principles study, J. Phys. Chem. C 125, 16955 (2021).
- [60] S. Sakong, D. Mahlberg, T. Roman, M. Pandey, and A. Groß, Influence of local inhomogenities and the

- electrochemical environment on the oxygen reduction reaction on Pt-based electrodes: A DFT study, J. Phys. Chem. C $\bf 124$, 27604 (2020).
- [61] G. Kresse and J. Furthmüller, Efficiency of ab-initio total energy calculations for metals and semiconductors using a plane-wave basis set, Comp. Mater. Sci. 6, 15 (1996).
- [62] G. Kresse and D. Joubert, From ultrasoft pseudopotentials to the projector augmented-wave method, Phys. Rev. B 59, 1758 (1999).
- [63] P. E. Blöchl, Projector augmented-wave method, Phys. Rev. B 50, 17953 (1994).
- [64] B. Hammer, L. B. Hansen, and J. K. Nørskov, Improved adsorption energetics within density-functional theory using revised perdew-burke-ernzerhof functionals, Phys. Rev. B 59, 7413 (1999).
- [65] J. P. Perdew, K. Burke, and M. Ernzerhof, Generalized gradient approximation made simple, Phys. Rev. Lett. 77, 3865 (1996).
- [66] S. Grimme, S. Ehrlich, and L. Goerigk, Effect of the damping function in dispersion corrected density functional theory, J. Comp. Chem. 32, 1456 (2011).
- [67] D. Mahlberg, S. Sakong, K. Forster-Tonigold, and A. Groß, Improved DFT adsorption energies with semiempirical dispersion corrections, J. Chem. Theory

- Comput. 15, 3250 (2019).
- [68] V. Wang, N. Xu, J.-C. Liu, G. Tang, and W.-T. Geng, Vaspkit: A user-friendly interface facilitating high-throughput computing and analysis using vasp code, Comp. Phys. Commun. 267, 108033 (2021).
- [69] J. K. Nørskov, T. Bligaard, A. Logadottir, J. R. Kitchin, J. G. Chen, S. Pandelov, and U. Stimming, Trends in the exchange current for hydrogen evolution, J. Electrochem. Soc. 152, J23 (2005).
- [70] J. K. Nørskov, J. Rossmeisl, A. Logadottir, L. Lindqvist, J. R. Kitchin, T. Bligaard, and H. Jónsson, Origin of the overpotential for oxygen reduction at a fuel-cell cathode, J. Phys. Chem. B 108, 17886 (2004).
- [71] C. Hou, G. Tai, Y. Liu, Z. Wu, X. Liang, and X. Liu, Borophene-based materials for energy, sensors and information storage applications, Nano Res. Energy 2, e9120051 (2023).
- [72] F. Gossenberger, F. Juarez, and A. Groß, Sulfate, bisulfate, and hydrogen co-adsorption on Pt(111) and Au(111) in an electrochemical environment, Front. Chem. 8, 634 (2020).
- [73] A. Groß, Reversible vs standard hydrogen electrode scale in interfacial electrochemistry from a theoretician's atomistic point of view, J. Phys. Chem. C 126, 11439 (2022).